

Convex Total Variation Denoising of Poisson Fluorescence Confocal Images With Anisotropic Filtering

Isabel Cabrita Rodrigues and João Miguel Raposo Sanches, *Member, IEEE*

Abstract—Fluorescence confocal microscopy (FCM) is now one of the most important tools in biomedicine research. In fact, it makes it possible to accurately study the dynamic processes occurring inside the cell and its nucleus by following the motion of fluorescent molecules over time. Due to the small amount of acquired radiation and the huge optical and electronics amplification, the FCM images are usually corrupted by a severe type of Poisson noise. This noise may be even more damaging when very low intensity incident radiation is used to avoid phototoxicity. In this paper, a Bayesian algorithm is proposed to remove the Poisson intensity dependent noise corrupting the FCM image sequences. The observations are organized in a 3-D tensor where each plane is one of the images acquired along the time of a cell nucleus using the fluorescence loss in photobleaching (FLIP) technique. The method removes simultaneously the noise by considering different spatial and temporal correlations. This is accomplished by using an anisotropic 3-D filter that may be separately tuned in space and in time dimensions. Tests using synthetic and real data are described and presented to illustrate the application of the algorithm. A comparison with several state-of-the-art algorithms is also presented.

Index Terms—Bayesian, convex optimization, denoising, laser scanning confocal fluorescence microscopy (LSCFM), Poisson.

I. INTRODUCTION

FLUORESCENCE confocal microscopy is nowadays one of the most important tools in biomedicine research. Because living tissues are very sensitive to wavelengths in the visible range causing damage in the microscopic living specimens, for a long time biomedical scientists conducted their research based upon dehydrated and chemically fixed specimens to guess on how living cells could function. In the second half of last century, microscopy methodologies experienced an extraordinary evolution due to the combination of the use of the physical phenomenon of fluorescence with the invention of the confocal

microscope (CM). These new tools opened a new perspective in the research of the dynamics of living cells.

The phenomenon of fluorescence, first reported in 1852 by Stokes, consists of the emission of light by excited fluorophore molecules within nanoseconds after the absorption of photons with a shorter wavelength, in order to reach the ground state. Nevertheless, the emission of fluorescence is not the only available mechanism fluorophore excited molecules make use for energy disposal. Fluorophores possess the ability to maintain for a relatively long time triplet excited states that favor the occurrence of photochemical reactions that irreversibly destroy their fluorescence. This phenomenon, called photobleaching, is in general an undesirable effect. Since all the fluorophores will eventually photobleach upon extended excitation, the image acquisition becomes more and more problematic as exposure time increases. However, some techniques such as fluorescence recovery after photobleaching (FRAP) and fluorescence loss in photobleaching (FLIP), take advantage of this not always merely damaging effect, to study some dynamic processes occurring inside the cells [1].

The first of the fluorescent proteins to be discovered was the green fluorescent protein (GFP) from Jellyfish *Aequorea Victoria*. The GFP can be incorporated as protein marker in the cell by a process of fusion of its coding sequence with the gene encoding the protein of interest, followed by stable or transient transfection into the cell with the purpose of inducing the production of a fusion protein to be used as an *in situ* fluorescent tag [2]. The tagged proteins can then be visualized in living cells in an almost noninvasive manner, without requiring prior fixation. The important role fluorescence techniques play in microscopy cause significant advances to occur since the last decade in this field with the development of synthetic probes and proteins.

The invention of the CM 50 years ago by M. Minsky was the other main ingredient that triggered the beginning of a new era in the research on the localization and dynamics of cellular proteins.

Confocal microscopy is an imaging technique that became a standard tool in biomedical sciences. The CM is designed to improve on the performance of the conventional optical microscope. A laser beam is reflected by a dichroic mirror and then highly focused by the objective lens to illuminate the point at focus inside the specimen, leaving the out-of-focus points much less illuminated. Before being collected, the emitted light typically with a longer wavelength than the incident radiation, goes through several optical filters and is refocused by the objective lens in an aperture, also called the pinhole, placed in front of

Manuscript received November 18, 2008; revised September 06, 2009 and May 16, 2010; accepted June 18, 2010. Date of publication July 08, 2010; date of current version December 17, 2010. This work was supported by FCT, under ISR/IST plurianual funding. The associate editor coordinating the review of this manuscript and approving it for publication was Prof. Peter C. Doerschuk.

I. C. Rodrigues is with Institute for Systems and Robotics, 1049-001 Lisbon, Portugal. She is also with Instituto Superior de Engenharia de Lisboa, 1049-001 Lisbon, Portugal.

J. M. R. Sanches is with Institute for Systems and Robotics, 1049-001 Lisbon, Portugal. He is also with Instituto Superior Técnico, 1049-001 Lisbon, Portugal.

Color versions of one or more of the figures in this paper are available online at <http://ieeexplore.ieee.org>.

Digital Object Identifier 10.1109/TIP.2010.2055879

the detector. This aperture, the optical filters and a beam-splitter, prevent the light emanating from the out-of-focus points, as well as the reflected radiation, from reaching the detector. The ability to select between in-focus and out-of-focus emitted light enables the acquisition of images of thin slices within the specimen volume. The laser scanning fluorescence confocal microscope (LSFCM) [3] is a more recent version of the CM that may include a wide spectrum of laser light sources coupled to highly accurate optoelectronic controlled filters. This microscope is also equipped with a scanner device to allow the acquisition of 2-D images, by scanning the focal point in the lateral direction.

Since the advent of the confocal microscopy methodologies, studies have been revealing a highly dynamic cellular environment [4]. Although the movement of the cellular structures can be tracked and quantified over time by means of the GFP-tagged proteins, the study of the dynamics of the individual component molecules inside the cell requires more sophisticated fluorescent imaging methods than simple time-lapse microscopy [5]. Techniques, such as FLIP and FRAP, make use of high intensity incident radiation as a perturbing agent of the distribution of fluorescent molecules in a sample. The occurrence of the photobleaching effect allows the analysis of the redistribution of the tagged particles of interest. In a FLIP experiment, during a certain time interval, a small defined region in the cell nucleus expressing fluorescently tagged proteins is illuminated with repetitive bleach pulses of a high intensity focused laser beam, to force the occurrence of the photobleaching effect. Remote regions of the nucleus are then monitored for the decrease in the fluorescence level. Any fraction of the cell nucleus connected to the area being bleached will gradually fade owing to the movement of the bleached molecules into the region. Thus, the rate of fluorescence loss and recovery is related to the mobility of the molecules inside the cell nucleus and can be the result of diffusion processes, chemical reactions and association or transport processes [3]. The resulting information from the experiment can then be used to determine the kinetic properties, including diffusion coefficients, mobile fraction and transport rate of the fluorescently labelled molecules.

Due to the small amount of detected radiation and the huge optical and electronics amplification, the LSFCM images may be considered as photon-limited, since the relatively small number of detected photons is the main factor limiting the signal-to-noise ratio (SNR). The data collected by these imaging systems exhibit a severe type of signal-dependent noise, usually assumed to obey a Poisson distribution, that must be attenuated before use by the biomedical researcher. In fact, an important task in image processing is denoising since the data measured by imaging instruments always contain noise and blur. Although it is unattainable to build devices that produce data with arbitrary fidelity, it is possible to mathematically reconstruct the underlying images from the corrupted data obtained from real-world instruments, so that information present but hidden in the data can be revealed with less blur and noise [6], [7].

Many image denoising algorithms are developed under the assumption of additive white Gaussian noise (AWGN), nevertheless the noise corrupting LSFCM images is assumed to be of Poisson type, whose main characteristic is its dependency upon

the image intensity. The denoising of such images is in general an ill-conditioned problem [8], requiring some sort of regularization that in that Bayesian framework is expressed in the form of a *a priori* distribution function. Several state-of-the-art approaches involve time consuming nonquadratic and nonnegatively constrained optimization algorithms, not suitable for large-scale real time applications.

Taking advantage of all the knowledge on AWGN denoising, some authors opt for modifying the Poisson statistics of the noisy observations by using a variance stabilizing transform (VST), such as the Anscombe¹ (Anscombe 1948) or the Fisz transforms [9], [10]. Most authors apply the Anscombe transform followed by a denoising/deconvolution methodology, giving rise to an AWGN linear algorithm whose solution is transformed back by using the inverse Anscombe transform. The drawback of this scheme is that the AWGN assumption is accurate when photon counts are larger than thirty [11] but inappropriate when counts drop to less than ten [12]. In a very recent work [13], the authors propose a deconvolution algorithm for blurred data contaminated by Poisson noise, where the Anscombe transform is included explicitly in the model, leading to a nonlinear formulation with additive Gaussian noise in the Bayesian *maximum a posteriori* (MAP) framework, with a nonsmooth regularizing term forcing sparsity over the representation coefficients of the image in a dictionary that includes wavelets, curvelets and their translation-invariant versions. A conjunction of a VST with wavelet, curvelet, ridgelet and other transforms is also used for Poisson noise removal in [14] and [15]. The resulting VST multiscale (MS) denoising approach achieves a good performance even in very low-count image situations.

The solution to these constrained image recovery problems, nested algorithms involving proximity operators [13], [16] seem to be very effective.

In the seventies, W.H. Richardson and L. Lucy, in separate works, developed a methodology specifically for data following a Poisson distribution. The Richardson–Lucy (R–L) algorithm can be viewed as an expectation-maximization (EM) algorithm including a Poisson statistical noise model. This algorithm presents several weaknesses, among them the noise amplification after a few iterations. However, this drawback can be avoided by introducing a regularization term. The (R–L) algorithm with total variation (TV) regularization was proposed in [17] for confocal microscopy imaging deconvolution. In [18], a prefiltering procedure to reduce noise before applying the R–L algorithm is presented. The use of the TV regularization in the presence of Poisson noise applied to astronomical image deconvolution is also examined in [19].

In this paper, we are dealing with the denoising problem of LSFCM images of human cell nucleus with the goal of estimating its morphology. The denoising problem is formulated in the Bayesian framework and conceived as an optimization task with the MAP criterion. Due to the resolution characteristics of the LSFCM, although blur is always present in the acquired im-

¹If Y is a Poisson random variable with intensity X , the Anscombe transform of Y , denoted by Z , is defined as $Z = A(Y) = 2\sqrt{Y + (3/8)}$. It can be shown that Z converges in distribution to a normal random variable with mean $2\sqrt{X}$ and unit variance as X increases.

ages, it is assumed here that blur can be neglected when compared to the exhibited noise. The morphology to be estimated is expected to consist of sets of homogeneous regions separated by well defined boundaries. In fact, if \mathbf{X} is the variable to be estimated using this framework, the knowledge of the main characteristics of the cell nucleus morphology is crucial to select the *a priori* distribution function $p(\mathbf{X})$, since it formalizes the expected joint behavior of the elements of \mathbf{X} . Due to the specific nature of the images under analysis, the local Markovianity of \mathbf{X} seems to be a reasonable assumption. The local Markovianity can be expressed as $p(x_i|x) = p(x_i|x_{N(i)})$, where x_i is the value of \mathbf{X} at the i th node² and $N(i)$ is the neighborhood of node i . According to the Hammersley–Clifford theorem [20] if the field \mathbf{X} has the local Markovianity property, then $p(\mathbf{X})$ can be written as a Gibbs distribution

$$p(\mathbf{x}) = \frac{1}{Z} \exp \left[- \sum_c V_c(\mathbf{x}) \right] \quad (1)$$

where Z is the partition function or normalizing constant, $V_c(\cdot)$ are the clique potentials [21] and $\sum_c V_c(\mathbf{x})$ is an energy that will be denoted by $E_X(\mathbf{X})$.

Once is the type of *a priori* distribution function selected, the second step consists on the choice of the most convenient clique potential functions to the problem. The literature on that subject is vast. Quadratic potentials have been by far the most commonly used. However, denoising with an *a priori* distribution based upon these potentials produces an over-smoothing of the discontinuities in the images. To overcome this difficulty, in the decades of 1980 and 1990 authors like Blake and Zisserman [22], Hebert and Leahy [23], Green [24], Geman, McClure and Geman [25], Geman and Reynolds [26], and Rudin, Osher, and Fatemi [27], proposed several convex and nonconvex discontinuity-preserving potentials.

In this paper, two denoising algorithms are proposed for LSFCM images where the FLIP technique is used. The goal is to provide biologists with better quality images to study the process of RNA molecule synthesis inside the cell nucleus, namely, their flow along time.

The denoising algorithms are formulated in the Bayesian framework where a Poisson distribution models the observation noise and a Gibbs distribution, with log-quadratic potential functions [28] in the first model and log-total variation (TV-log) and log-quadratic potential functions in the second model, regularizes the solution, thus, defining the field to be estimated as a Markov random field (MRF). These potential functions have shown to be more appropriated to deal with this type of optimization problems in R_+^N [28]. The regularization is performed simultaneously in the image space and in time (time courses) but using different *a priori* distributions. The denoising iterative algorithm involves an anisotropic 3-D filtering process to cope with the different smoothing effects performed in the space and time dimensions. Tests using synthetic and real data are presented to illustrate the application of the algorithm.

The paper is organized as follows. In Section II, the problem is formulated from a mathematical point of view, Section III

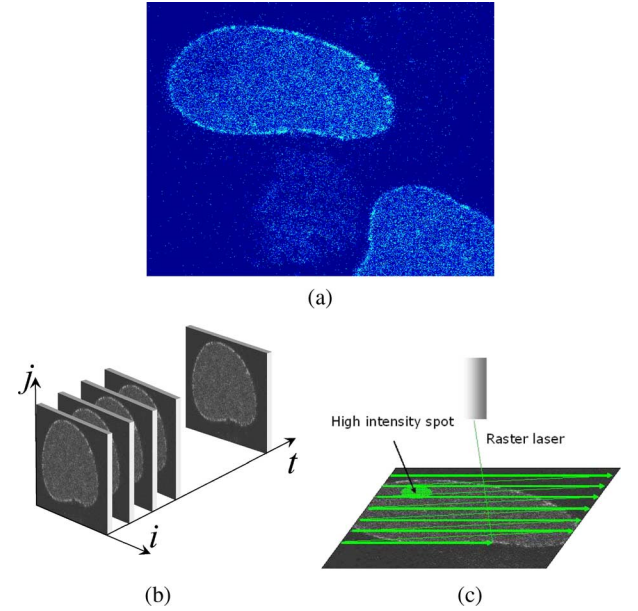


Fig. 1. LSFCM. (a) Low SNR LSFCM image corrupted with pixel dependent noise. (b) Temporal image sequence. (c) FLIP technique.

gives a brief review of the Graph-Cuts labelling methodology and Section IV presents the experimental results using synthetic and real data. A comparison with five state-of-the-art algorithms is also presented. Section V concludes the paper.

II. PROBLEM FORMULATION

Each sequence of LSFCM images under analysis, \mathbf{Y} , corresponds to L observations of a cell nucleus acquired along the imaging time [Fig. 1(b)] by using the FLIP technique [Fig. 1(c)]. Data can be represented as a 3-D tensor, $\mathbf{Y} = \{y_{i,j,t}\}$, with $0 \leq i, j, t \leq N - 1, M - 1, L - 1$. Each data point, $y_{i,j,t}$, is corrupted with Poisson noise which means that each image at the discrete time t_k , $y(i, j, t_k)$ and each time course $y(i_k, j_k, t)$ are corrupted with Poisson noise. The ultimate goal of the proposed algorithms is to estimate the underlying cell nucleus morphology, \mathbf{X} , from these noisy data, \mathbf{Y} , exhibiting a very low SNR. Fig. 1(a) shows a low SNR LSFCM image from a real sequence.

A Bayesian approach using the MAP criterion is adopted to estimate \mathbf{X} . This problem may be formulated as the following energy optimization task:

$$\hat{\mathbf{X}} = \arg \min_{\mathbf{X}} E(\mathbf{X}, \mathbf{Y}) \quad (2)$$

where the energy function $E(\mathbf{X}, \mathbf{Y}) = E_Y(\mathbf{X}, \mathbf{Y}) + E_X(\mathbf{X})$ is a sum of two terms, $E_Y(\mathbf{X}, \mathbf{Y})$ called the data fidelity term and $E_X(\mathbf{X})$ called the energy associated to the *a priori* distribution. The first term pushes the solution toward the observations according to the type of noise corrupting the images and the second term penalizes the solution according to some previous knowledge about \mathbf{X} [29], [30]. This prior term regularizes the solution and helps to remove the noise.

²The lattice where the sequence of images lies is regarded as a graph where each variable is assigned to a node.

If independence of the observations is assumed, the data fidelity term, which is the anti-logarithm of the likelihood function, is defined as follows:

$$E_Y(\mathbf{X}, \mathbf{Y}) = -\log \left[\prod_{i,j,t=0}^{N-1,M-1,L-1} p(y_{i,j,t} | x_{i,j,t}) \right] \quad (3)$$

where $p(y|x) = (x^y/y!)e^{-x}$ is the Poisson distribution, leading to

$$E_Y(\mathbf{X}, \mathbf{Y}) = \sum_{i,j,t=0} [x_{i,j,t} - y_{i,j,t} \log(x_{i,j,t})] + C \quad (4)$$

where C is a constant term.

In the proposed algorithms, anisotropic *a priori* terms are used, in the sense that correlations in the spatial and temporal dimensions are different.

Assuming \mathbf{X} as MRF, $p(\mathbf{X})$ is given by (1). One of the most popular potential functions is the quadratic, mainly for the sake of mathematic simplicity. However, these functions over-smooth the solution attenuating relevant details. To overcome this difficulty, edge preserving *a priori* potentials are more convenient and have been described in the literature, as referred in Section I. The TV based Gibbs energy has been used successfully in several problems [8], [27], [31]–[37].

Recently, a new type of potential functions was proposed in [28]. This new class of functions, instead of using differences between neighbors, uses logarithms of ratios which means differences of logarithms, allowing the interpretation of differences between neighbors in terms of the order of magnitude. This new approach was chosen because it simplifies the calculus and also because it is suitable to be used when the unknowns to be estimated are all positive [28].

In this paper, emphasis to the choice of the *a priori* distribution functions in the space and in the time dimensions, is given. For comparison purposes, four potential functions [(5) to (8)] are plotted in Fig. 2. These plots help to understand which potentials are more suitable to each dimension. Functions (5) and (6) are based upon the well known L_1 and L_2 norms that are extensively used in the literature. The other two, (7) and (8), are used in this paper. $x - \zeta$ is to be interpreted as a difference of intensities between neighboring pixels. ζ was set constant and positive, equal to one in all the equations for simplicity

$$L_1 \propto |x - \zeta| \quad (5)$$

$$L_2 \propto (x - \zeta)^2 \quad (6)$$

$$L_2 \log \propto \log^2 \left(\frac{x}{\zeta} \right) \quad (7)$$

$$TV \log \propto \sqrt{\log^2 \left(\frac{x}{\zeta} \right)}. \quad (8)$$

As can be noticed in Fig. 2, the L_2 function, associated with the quadratic potential, imposes a large penalization to large values of x , which corresponds to a severe smoothing of significant transitions. That is the reason why the quadratic potential function is appropriated for use in the time dimension,

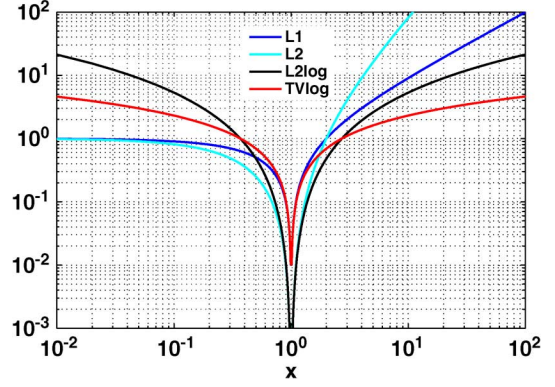


Fig. 2. L_1 , L_2 , $L_2 \log$ and $TV \log$ *a priori* potentials.

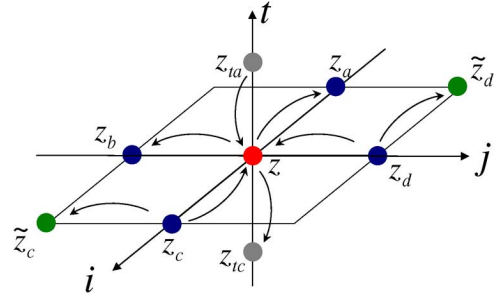


Fig. 3. Neighboring system.

where no abrupt transitions are expected but, when used in the space dimension, it leads to a loss of morphological details, as will be analyzed later. The L_1 is less severe when considering large values of x and presents almost the same behavior as L_2 for small values of x . The $L_2 \log$ imposes even less smoothing to high values of x , but for small values of x it is much more severe than the previous ones, which leads to an efficient high frequency noise removal in homogeneous regions. For large values of x the $TV \log$ functions assume smaller values than the $L_2 \log$, which means less penalization of the sharp transitions. This seems an interesting feature to take into account when considering the regularization on the space dimensions.

In this paper, a novel potential function to model the spatial correlation, called $TV \log$, is presented

$$V_c(x, y, z) = \sqrt{\log^2 \left(\frac{x}{y} \right) + \log^2 \left(\frac{x}{z} \right)} \quad (9)$$

where x, y, z are nodes belonging to a 2-D second-order clique as displayed in Fig. 3.

Two denoising algorithms are proposed for LSFCM images where the FLIP technique is used. The algorithms that will be denoted by $L_2 L_2 \log$ (A in the equations) and $TV L_2 \log$ (B in the equations), are formulated in the Bayesian framework. A Poisson distribution models the observation noise and Gibbs distributions ((1)) with log-quadratic potential functions in space and in time for the $L_2 L_2 \log$ model, and TV -log potential functions in space and log-quadratic potential functions in time for the $TV L_2 \log$ model. Edge preserving priors in the time domain are not needed because abrupt changes in the time courses are not supposed to occur. In fact, the expected

evolution of each time course is like an exponential decay that results from the photobleaching and diffusion effects.

The energy functions related to the *a priori* distributions are given by

$$E_{X_A}(X) = \alpha \sum_{i,j,t} \left[\log^2 \left(\frac{x_{i,j,t}}{x_{i-1,j,t}} \right) + \log^2 \left(\frac{x_{i,j,t}}{x_{i,j-1,t}} \right) \right] + \beta \sum_{i,j,t} \log^2 \left(\frac{x_{i,j,t}}{x_{i,j,t-1}} \right) \quad (10)$$

for the L_2L_2 log model and

$$E_{X_B}(X) = \alpha \sum_{i,j,t} \sqrt{\log^2 \left(\frac{x_{i,j,t}}{x_{i-1,j,t}} \right) + \log^2 \left(\frac{x_{i,j,t}}{x_{i,j-1,t}} \right)} + \beta \sum_{i,j,t} \log^2 \left(\frac{x_{i,j,t}}{x_{i,j,t-1}} \right) \quad (11)$$

for the TVL_2 log model, where α and β are strictly positive prior parameters to tune the level of smoothing across the images and across the time courses, respectively.

Therefore, the overall problem consists on the minimization of the following functions:

$$E_A(\mathbf{X}, \mathbf{Y}) = \sum_{i,j,t=0}^{N-1,M-1,L-1} [x_{i,j,t} - y_{i,j,t} \log(x_{i,j,t})] + \alpha \sum_{i,j,t} \left[\log^2 \left(\frac{x_{i,j,t}}{x_{i-1,j,t}} \right) + \log^2 \left(\frac{x_{i,j,t}}{x_{i,j-1,t}} \right) \right] + \beta \sum_{i,j,t} \log^2 \left(\frac{x_{i,j,t}}{x_{i,j,t-1}} \right) \quad (12)$$

for the L_2L_2 log model and

$$E_B(\mathbf{X}, \mathbf{Y}) = \sum_{i,j,t} [x_{i,j,t} - y_{i,j,t} \log(x_{i,j,t})] + \alpha \sum_{i,j,t} \sqrt{\log^2 \left(\frac{x_{i,j,t}}{x_{i-1,j,t}} \right) + \log^2 \left(\frac{x_{i,j,t}}{x_{i,j-1,t}} \right)} + \beta \sum_{i,j,t} \log^2 \left(\frac{x_{i,j,t}}{x_{i,j,t-1}} \right) \quad (13)$$

for the TVL_2 log model.

Both minimization tasks (12), (13) lead to nonconvex problems [38] and their optimization using gradient descent or Newton's [39] based methods is difficult. The nonconvexity of these functions comes from the fact that they are sums of convex functions with nonconvex ones, e.g., $\sqrt{\log^2(x)}$.

However, by performing an appropriate change of variable it is possible to turn them into convex. Let us consider the following variable changing $z = g(x) = \log(x)$, which leads to $z_{i,j,t} = \log(x_{i,j,t})$ or $x_{i,j,t} = e^{z_{i,j,t}}$. The function $g(x)$

is monotonic and, therefore, the minimizers of $E(\mathbf{X}, \mathbf{Y})$ and $E(\mathbf{Z}, \mathbf{Y})$ are related by $\mathbf{Z}^* = \log(\mathbf{X}^*)$.

The new objective functions for the models are

$$E_A(\mathbf{Z}, \mathbf{Y}) = \sum_{i,j,t} [e^{z_{i,j,t}} - y_{i,j,t} z_{i,j,t}] + \alpha \sum_{i,j,t} (z_{i,j,t} - z_{i-1,j,t})^2 + (z_{i,j,t} - z_{i,j-1,t})^2 + \beta \sum_{i,j,t} (z_{i,j,t} - z_{i,j,t-1})^2 \quad (14)$$

$$E_B(\mathbf{Z}, \mathbf{Y}) = \sum_{i,j,t} [e^{z_{i,j,t}} - y_{i,j,t} z_{i,j,t}] + \alpha \sum_{i,j,t} \sqrt{(z_{i,j,t} - z_{i-1,j,t})^2 + (z_{i,j,t} - z_{i,j-1,t})^2} + \beta \sum_{i,j,t} (z_{i,j,t} - z_{i,j,t-1})^2. \quad (15)$$

The minimization of (14) and (15) is performed by finding their stationary points according to the condition

$$\nabla E(\mathbf{Z}, \mathbf{Y}) = 0. \quad (16)$$

Here, the optimization of $E(\mathbf{Z}, \mathbf{Y})$ is performed by using the iterated conditional modes (ICM) method [20], where the multivariate energy function $E(\mathbf{Z}, \mathbf{Y})$ is optimized in an element-wise basis. In this method, the optimization of $E(\mathbf{Z}, \mathbf{Y})$ is iteratively performed with respect to each component $z_{i,j,t}$ at a time, considering all other components as constants in each iteration.

A. L_2L_2 log Model

For the L_2L_2 log model the stationary point condition leads to

$$\frac{\partial E_A(\mathbf{Z}, \mathbf{Y})}{\partial z_{i,j,t}} = e^{z_{i,j,t}} - y_{i,j,t} + (h_A)_{i,j,t} \quad (17)$$

with $0 \leq i, j, t \leq N-1, M-1, L-1$ and where

$$(h_A)_{i,j,t} = 2\alpha \left[N_s z_{i,j,t} - \sum_s (z_s)_{i,j,t} \right] + 2\beta \left[N_t z_{i,j,t} - \sum_\tau (z_\tau)_{i,j,t} \right] \quad (18)$$

and $(z_s)_{i,j,t}$ and $(z_\tau)_{i,j,t}$ are the $N_s = 4$ spatial and $N_t = 2$ temporal neighbors of $z_{i,j,t}$, respectively.

The elements $(h_A)_{i,j,t}$ are organized in the tensor $\mathbf{H}_A = \{(h_A)_{i,j,t}\}$ which may be computed by

$$\mathbf{H}_A = \Phi_A * \mathbf{Z} \quad (19)$$

where $*$ denotes the 3-D convolution and Φ_A is the following 3-D mask:

$$\Phi_A = 2 \begin{pmatrix} 0 & 0 & 0 \\ 0 & -\beta & 0 \\ 0 & 0 & 0 \\ \hline 0 & -\alpha & 0 \\ -\alpha & \alpha N_s + \beta N_t & -\alpha \\ \hline 0 & -\alpha & 0 \\ 0 & 0 & 0 \\ 0 & -\beta & 0 \\ 0 & 0 & 0 \end{pmatrix}. \quad (20)$$

The solution of (16) is obtained by solving the convex equation

$$F(\mathbf{Z}) = e^{\mathbf{Z}} - \mathbf{Y} + \mathbf{H}_A = \mathbf{0} \quad (21)$$

using straightforward the Newton method

$$\mathbf{Z}^{(k+1)} = \mathbf{Z}^{(k)} - \left(e^{\mathbf{Z}^{(k)}} - \mathbf{Y} + \mathbf{H}_A^{(k)} \right) \oslash \mathbf{V}^{(k)} \quad (22)$$

where $\mathbf{V}^{(k)} = \{v_{i,j,t}^k\}$, $v_{i,j,t}^k = e^{z_{i,j,t}^k} + 2(\alpha N_s + \beta N_t)$, k stands for the iteration number and \oslash is the notation for the Hadamard element-wise division. Reversing the change of variable, the final solution is

$$\hat{\mathbf{X}} = e^{\hat{\mathbf{Z}}}. \quad (23)$$

B. TVL₂ log Model

The minimization of (15) is difficult from a numerical point of view due the nonquadratic TV terms and the reweighted least squares (RWLS) [29], [40] method used.

The convergence analysis of this method is long, out of the scope of this paper and it is treated in detail in [41]. However, in general terms, the convergence of this algorithm depends upon the choice of the prior parameters α and β . The smaller the parameters, the more unstable the iterative algorithm becomes from a numerical point of view. Here the prior parameters are chosen by the user to obtain the desired regularization effect and lead to convergence.

Let us consider the terms of the energy function (15) involving a given node $z = z_{i,j,t}$

$$\begin{aligned} E_B(z) = & e^z - yz + \alpha \left[\sqrt{(z - z_a)^2 + (z - z_b)^2} \right. \\ & + \sqrt{(z - z_c)^2 + (z_c - \tilde{z}_c)^2} \\ & \left. + \sqrt{(z - z_d)^2 + (z_d - \tilde{z}_d)^2} \right] \\ & + \beta \left[(z - z_{tc})^2 + (z - z_{ta})^2 \right] + C \end{aligned} \quad (24)$$

where z_a, z_b, z_c, z_d are the spatial neighbors of z and \tilde{z}_c and \tilde{z}_d are neighbors of z_c and z_d , respectively; z_{tc} and z_{ta} are the causal and anti-causal temporal neighbors of z , respectively (see Fig. 3); C is a term that does not depend upon z .

The minimizer of the convex energy function (24), z^* , is also the minimizer of the following energy function with quadratic terms associated with the spatial interaction:

$$\begin{aligned} \tilde{E}_B(z, z^*) = & e^z - yz + \alpha \left[w(z^*) \left((z - z_a)^2 + (z - z_b)^2 \right) \right. \\ & + w_c(z^*) \left((z - z_c)^2 + (z_c - \tilde{z}_c)^2 \right) \\ & \left. + w_d(z^*) \left((z - z_d)^2 + (z_d - \tilde{z}_d)^2 \right) \right] \\ & + \beta \left[(z - z_{tc})^2 + (z - z_{ta})^2 \right] \end{aligned} \quad (25)$$

where

$$w(z) = \frac{1}{\sqrt{(z - z_a)^2 + (z - z_b)^2}} \quad (26)$$

$$w_c(z) = \frac{1}{\sqrt{(z - z_c)^2 + (z_c - \tilde{z}_c)^2}} \quad (27)$$

$$w_d(z) = \frac{1}{\sqrt{(z - z_d)^2 + (z_d - \tilde{z}_d)^2}}. \quad (28)$$

The weights $w(z^*)$, $w_c(z^*)$ and $w_d(z^*)$ needed to compute (25) are not known because they depend upon the minimizer z^* , to be computed. Thus, an iterative strategy is used where in each k th iteration the previous estimation of z^* , z^{k-1} , is used to compute the weights $w(z^{k-1})$, $w_c(z^{k-1})$ and $w_d(z^{k-1})$. The minimization of (24) is iteratively performed as follows:

$$z^k = \arg \min_z \tilde{E}_B(z, z^{k-1}). \quad (29)$$

This minimization task with respect to $z_{i,j,t}$ is accomplished by finding the stationary point of $\tilde{E}_B(z, z^{k-1})$

$$\nabla \tilde{E}_B(z, z^{k-1}) = 0 \quad (30)$$

which is equivalent to compute the zero of the following function:

$$f_{i,j,t} = e^{z_{i,j,t}} - y_{i,j,t} + (h_B)_{i,j,t} = 0 \quad (31)$$

where

$$\begin{aligned} (h_B)_{i,j,t} = & 2\alpha \left[2w_{i,j,t} + w_{c_{i,j,t}} + w_{d_{i,j,t}} \right] z_{i,j,t} \\ & - 2\alpha \left\{ w_{i,j,t} [z_{i-1,j,t} + z_{i,j-1,t}] + w_{c_{i,j,t}} z_{i+1,j,t} \right. \\ & \left. + w_{d_{i,j,t}} z_{i,j+1,t} \right\} \\ & + 2\beta \left[N_t z_{i,j,t} - \sum_{\tau} (z_{\tau})_{i,j,t} \right] \end{aligned} \quad (32)$$

$(z_{\tau})_{i,j,t}$ are the $N_t = 2$ temporal neighbors of $z_{i,j,t}$ and

$$\begin{aligned} w_{i,j,t} = & \frac{1}{\sqrt{(z_{i,j,t} - z_{i-1,j,t})^2 + (z_{i,j,t} - z_{i,j-1,t})^2}} \\ w_{a_{i,j,t}} = & \frac{1}{\sqrt{(z_{i+1,j,t} - z_{i,j,t})^2 + (z_{i+1,j,t} - z_{i+1,j-1,t})^2}} \\ w_{c_{i,j,t}} = & \frac{1}{\sqrt{(z_{i,j+1,t} - z_{i-1,j+1,t})^2 + (z_{i,j+1,t} - z_{i,j,t})^2}}. \end{aligned}$$

In matrix notation the whole set of (31) can be written as follows:

$$F(\mathbf{Z}) = e^{\mathbf{Z}} - \mathbf{Y} + \mathbf{H}_B = 0 \quad (33)$$

where the tensor $\mathbf{H}_B = \{(h_B)_{i,j,t}\}$ may be computed by

$$\mathbf{H}_B = \Phi_B * \mathbf{Z}. \quad (34)$$

The $3 \times 3 \times 3$ dimensional tensor Φ_B is a spatiotemporal varying 3-D mask defined as follows:

$$(\Phi_B)_{i,j,t} = 2 \begin{pmatrix} 0 & 0 & 0 \\ 0 & -\beta & 0 \\ 0 & 0 & 0 \\ \hline 0 & -\alpha w_{i,j,t} & 0 \\ -\alpha w_{i,j,t} & \phi_{i,j,t} & -\alpha w_{d_{i,j,t}} \\ 0 & -\alpha w_{c_{i,j,t}} & 0 \\ \hline 0 & 0 & 0 \\ 0 & -\beta & 0 \\ 0 & 0 & 0 \end{pmatrix} \quad (35)$$

where $\phi_{i,j,t} = \alpha[2w_{i,j,t} + w_{c_{i,j,t}} + w_{d_{i,j,t}}] + \beta N_t$.

Notice that in this TVL_2 log model the 3-D mask, Φ_B varies along the time and the space, contrary to what occurs in the L_2L_2 log model where Φ_A is constant.

Using again the Newton's method the solution of (33) is attained by

$$\mathbf{Z}^{(k+1)} = \mathbf{Z}^{(k)} - \left(e^{\mathbf{Z}^{(k)}} - \mathbf{Y} + \mathbf{H}_B^{(k)} \right) \oslash \mathbf{V}^{(k)} \quad (36)$$

where $\mathbf{V}^{(k)} = \{v_{i,j,t}^k\}$ with

$$v_{i,j,t}^k = e^{z_{i,j,t}^{(k)}} + 2\alpha \left(2w_{i,j,t}^k + w_{c_{i,j,t}}^k + w_{d_{i,j,t}}^k \right) + 2\beta N_t. \quad (37)$$

Reversing the change of variable, the final solution is

$$\hat{\mathbf{X}} = e^{\hat{\mathbf{Z}}}. \quad (38)$$

A straightforward extension of these models to cope with blur is feasible but is mathematically and computationally demanding. In this case, it seems that a 2-step iterative methodology could be an interesting alternative, where in each iteration the first step consists of applying a deconvolution algorithm to the data and in the second step the denoising of the deblurred data is performed until some stopping criteria is met.

III. LABELLING

The FLIP technique [see Fig. 1(c)] adopted to generate the data used in this paper is appropriated to study the flow dynamics inside the cell nucleus. By strongly bleaching a small spot at a given location in the nucleus, the GFP molecules entering in the spot region are turned off by losing their ability to fluoresce due the photobleaching effect [3]. The average intensity of the image decreases and the bleached spot is the source of this decrease. The evolution of the intensity decreasing across the cell nucleus allows the analysis of the diffusion process involved, as well as the inference of the dynamics and mobility of

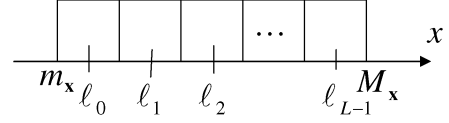


Fig. 4. Labels.

the GFP molecules which are usually bonded to other biologically relevant molecules, e.g., RNA molecules.

In this section, the diffusion process is visualized by thresholding the images according to its intensity along the time courses in order to observe the propagation process of intensity decreasing across the cell nucleus that started at the bleached region.

In this approach, the evolution of the boundaries on the binary image for a given threshold gives the information about the propagation process. To observe this process at several locations different thresholds are used simultaneously by extending the previous binary strategy to a multilabel methodology.

This segmentation methodology produces a labelling field $\mathcal{L} = \{\ell(n)\}$ where the label, $\ell(n)$, associated with each denoised pixel $x(n)$ is computed as

$$\hat{\ell}(n) = \arg \min_{\ell(n) \in \ell_0, \dots, \ell_{L-1}} |x(n) - \ell(n)| \quad (39)$$

where L is the number of labels and

$$\ell_i = m_x + \frac{2i+1}{2L}(M_x - m_x), \quad 0 \leq i \leq L-1 \quad (40)$$

is the center of the i th interval, as shown in Fig. 4. M_x and m_x are the maximum and the minimum values of $\mathbf{X} = \{x(n)\}$, respectively, and $n = \{i, j, t\}$ is the index of each pixel at the t th instant.

This labelling scheme produces clusters made of pixels with intensities in given ranges that evolve along the time courses, providing information about the diffusion process. However, this method does not favor piecewise constant clusters because it does not take into account spatial interactions between neighboring pixels. Therefore, a segmentation process is proposed based upon the following optimization task

$$\hat{\mathcal{L}} = \arg \min_{\mathcal{L}} E(\mathbf{X}, \mathcal{L}) \quad (41)$$

where

$$E(\mathbf{X}, \mathcal{L}) = \sum_n |\ell(n) - x(n)| + \sum_n [V(\ell(n), \ell_v(n)) + V(\ell(n), \ell_h(n))]. \quad (42)$$

$\ell_v(n)$ and $\ell_h(n)$ are the labels associated with the vertical and horizontal causal neighboring pixels of $x(n)$ and $V(\ell_a, \ell_b)$ is a function that penalizes different labels in neighboring nodes. The first term of $E(\mathbf{X}, \mathcal{L})$ pushes the solution toward the thresholding result given by (39) while the second, called regularization term, promotes the homogeneity of the labelled regions

by eliminating outliers and small regions out of context. The penalty function is defined as follows:

$$V(\ell_a, \ell_b) = \begin{cases} 0, & \text{if } \ell_a = \ell_b \\ \alpha / (\tilde{g}(n) + \epsilon), & \text{otherwise} \end{cases} \quad (43)$$

where $\tilde{g}(n)$ is the normalized ($0 \leq \tilde{g}(n) \leq 1$) gradient of \mathbf{X} at the n th pixel and $\epsilon = 10^{-6}$ is a small number to avoid division by zero. This penalization function is used to penalize different neighboring labels and promote piecewise constant labelled regions.

The gradient of \mathbf{X} at the n th pixel is $g(n) = \sqrt{(x(n) - x_v(n))^2 + (x(n) - x_h(n))^2}$ where $x_v(n)$ and $x_h(n)$ are the vertical and horizontal causal neighboring pixels of $x(n)$. In homogeneous regions of \mathbf{X} , the normalized gradient is close to zero and the penalization term is large to force labeling homogeneity. On the contrary, when the gradient is large the penalization decreases in order to preserve the transitions. The parameter α , manually tuned, is used to control the strength of spatial correlation. When $\alpha = 0$ the solutions of (39) and (41) coincide.

The minimization of (42), formulated in (41), is performed in an image by image basis and is a huge optimization task performed in the Ω^{NM} high-dimensional space where $\Omega = \{0, 1, \dots, L-1\}$ is the set of labels and N and M are the dimensions of the images.

In [42] the authors have shown that several high-dimensional combinatorial optimization problems can be efficiently solved by using graph-cuts (GraphC) based algorithms. The authors have designed a very fast and efficient algorithm based upon the max-flow min-cut theorem [43] to compute the optimal solution of the energy function, that is, the global minimum. However, the algorithm is not completely general which means that some energy functions cannot be minimized with the proposed method. In [44], the authors present a wide class of energy functions that may be minimized with the GraphC method and the function (42) belongs to that class. In this paper, the minimization of (43) is performed by using the graph cut based method proposed in [42].

IV. EXPERIMENTAL RESULTS

In this section, results using synthetic and real data are presented. The synthetic data are used to characterize the performance of the proposed algorithms. The TVL_2 log model is compared to five state-of-the-art algorithms. Real image sequences are used to illustrate the application of the presented algorithms. The denoised images are segmented using the labelling algorithm to represent the diffusion process involved in the FLIP technique of fluorescence image acquisition.

A. Synthetic Data

In order to assess the performance of the proposed denoising methodologies described previously, synthetic data were generated and processed. Three 64×64 pixels initial images with a cell nucleus shape were formed, each exhibiting three intensity levels in three different regions corresponding to the background of the image, to the cell nucleus and to the bleached area, according to Table I, with the aim of studying the behavior of

TABLE I
SYNTHETIC DATA. SEQUENCES *sint1*, *sint2* AND *sint3*. INTENSITY VALUES USED TO GENERATE THE INITIAL IMAGES, UPON WHICH EXPONENTIAL DECAYS ALONG THE TIME COURSES ARE APPLIED TO SIMULATE THE PHOTBLEACHING EFFECT, FOR EACH OF THE THREE SYNTHETIC SEQUENCES

Sequence	Background	Nucleus shape area	Dark circle (bleached area)
<i>sint1</i>	0.06	2	0.6
<i>sint2</i>	0.6	20	6
<i>sint3</i>	6	200	60

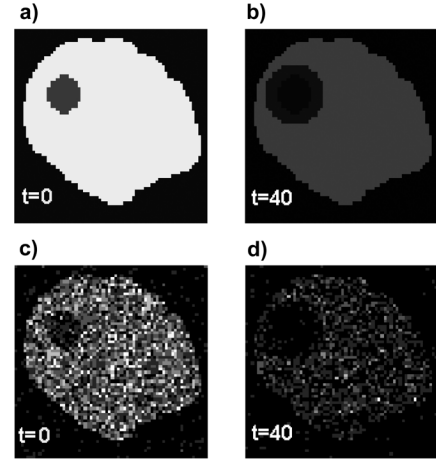


Fig. 5. Synthetic data: (a) and (b) true; (c) and (d) noisy, for $t = 0$ and $t = 40$ (image time).

the proposed algorithms in different 2-D signal-to-noise ratio (2-D-SNR) situations. The 2-D-SNR is SNR computed for each image in the sequence. The values in Table I were set to simulate the orders of magnitude of the intensity ratios among the background, the nucleus and the bleached area in a true FLIP experiment. Since Poisson noise is pixel intensity dependent, different intensity ranges allow the generation of data sets with dissimilar SNR values. In this experiment, three data sets were generated making use of the intensity values presented in Table I. To each pixel of the initial images, an exponential decay along the time courses ($t = 0, \dots, 63$) was applied to simulate the intensity decrease due to the photobleaching effect in a FLIP experiment, with rates equal to 0.07 for every pixel in the range of 10 (in pixel units) from the center coordinates of the dark circle and equal to 0.02 for the rest of the image. The obtained true sequences were then corrupted with Poisson noise. The resulting three synthetic sequences, named *sint1*, *sint2* and *sint3* exhibit, respectively, the following SNR ranges: -5 dB to 3 dB, 3 dB to 13 dB, and 14 dB to 23 dB.

Fig. 5 shows an example of two original noiseless images and their noisy versions in two different time instants, from one of the synthetic sequences.

The sequences were processed using both denoising algorithms described in this paper, the L_2L_2 log and the TVL_2 log.

The prior parameters α and β were tuned to take into account the intensity ranges in each sequence and image according to the empirical formulæ

$$\alpha(t) = \alpha_0 \times \frac{\bar{y}(t)}{std(y(t))} \quad (44)$$

TABLE II
 α_0, β_0 , CPU TIME (s) TO PROCESS THE COMPLETE SEQUENCE, NUMBER OF
 ITERATIONS USED IN DENOISING PROCEDURE OF THE SYNTHETIC SEQUENCES
 WITH THE STOPPING CRITERION: rel. error $\leq 5 \times 10^{-4}$

Algorithm	sequence	α_0	β_0	CPU (s)	#Iter.
TVL_2 log	<i>sint1</i>	0.25	10	40.5	263
	<i>sint2</i>	0.7	35	37.3	245
	<i>sint3</i>	2.5	100	31.4	210
L_2L_2 log	<i>sint1</i>	1.75	8	26.7	485
	<i>sint2</i>	2	24	27.8	493
	<i>sint3</i>	2.5	80	25.4	490

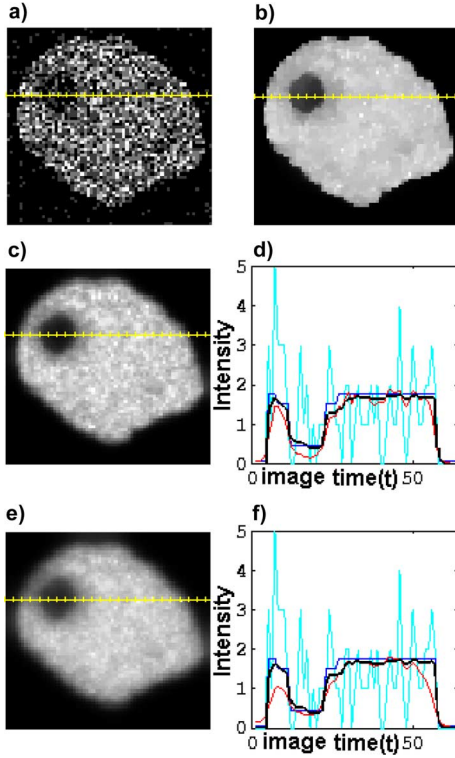


Fig. 6. Synthetic data *sint1* with low initial 2-D-SNR: -5 dB to 3 dB. (a) Noisy. (b) TVL_2 log. (c) L_2L_2 log with $\alpha = 1, \beta = 8$. (e) L_2L_2 log with $\alpha = 10, \beta = 80$. (d) and (f) Horizontal profiles along the yellow line in (a). The cyan line stands for the raw data, the red line for the L_2L_2 log model, the black line for TVL_2 log model, and the blue line corresponds to the original true data.

and

$$\beta(t) = \beta_0 \times \frac{\bar{y}(t)}{std(y(t))} \quad (45)$$

where $\bar{y}(t)$ and $std(y(t))$ are the average intensity and standard deviation of the t th image in sequence, respectively. α_0 and β_0 are constants manually adjusted in a trial and error basis.

The stopping criterion was based upon a measure of the relative error between iterations, computed as rel. error = $(\|z^k - z^{k-1}\| / \|z^k\|) \leq 5 \times 10^{-4}$.

The values of the tuning parameters α_0, β_0 , the number of iterations and the CPU time (in a Centrino Duo 2.00 GHz, 1.99 GB RAM processor) required to process each sequence according to the stopping criterion are displayed in Table II.

Figs. 6 and 7 show noisy (a) and denoised images from sequences *sint1* and *sint3* at the same time instant, using the

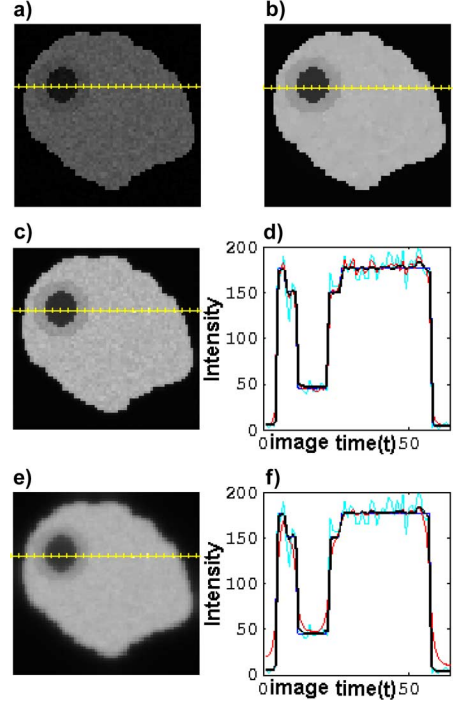


Fig. 7. Synthetic data *sint3* with high initial 2-D-SNR: 14 dB to 23 dB. (a) Noisy. (b) TVL_2 log. (c) L_2L_2 log with $\alpha = 2, \beta = 50$. (e) L_2L_2 log with $\alpha = 20, \beta = 500$. (d) and (f) Horizontal profiles along the yellow line in (a). The cyan line stands for the raw data, the red line for the L_2L_2 log model, the black line for TVL_2 log model, and the dark blue line corresponds to the original true data.

TVL_2 log model (b), and the L_2L_2 log model (c) and (e); (d) and (f) show the respective profiles taken along the yellow line in (a), where the cyan line stands for the raw data, the red line for the L_2L_2 log model, the black line for TVL_2 log model and the blue line corresponds to the original true data. In these figures, two versions of denoised images with model L_2L_2 log are presented (c and (e). In (c) and in profile (d), the prior parameters (α and β in (14)) were selected in order to achieve results at the transitions similar to the ones obtained with the TVL_2 log model. As it can be observed, the L_2L_2 log results in (c) and (d) (red line) are noisier than the ones obtained with the TVL_2 log model in (b) and (d) (black line). On the other hand, in version (e) and profile (f) the prior parameters of the L_2L_2 log model were increased to reduce the noise to a level comparable to the one attained with model TVL_2 log, which leads to a deterioration of the sharpness of the transitions and consequently a loss of details in the images.

The observation of the profile plots (d) and (f) makes evident the edge preserving ability of model TVL_2 log when compared to model L_2L_2 log, particularly in the case of strong space regularization (high values of α in model L_2L_2 log—images (e) in Figs. 6 and 7), which confirms the initial assumption that an edge preserving prior in the space domain is needed to keep transitions. Also in the profile plots, blue and black lines are almost indistinguishable, result of the good denoising quality attained by the TVL_2 log model.

Fig. 8 shows plots of the 2-D-SNR versus image time for each sequence before and after the sequences denoising. As seen in the figure, for all intensity ranges the 2-D-SNR values obtained

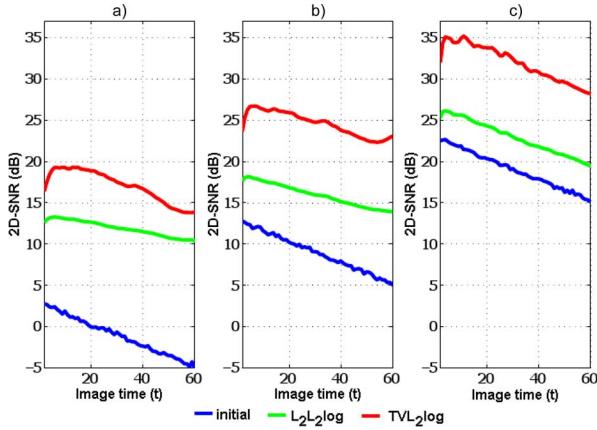


Fig. 8. 2-D-SNR before and after denoising sequences *sint1*, *sint2* and *sint3* with models $L_2L_2 \log$ and $TVL_2 \log$ versus image time plots. Synthetic data: (a) *sint1* with low 2-D-SNR; (b) *sint2* with medium 2-D-SNR; and (c) *sint3* with high 2-D-SNR. The horizontal axis represents the image time in the sequence. Blue lines stand for the initial 2-D-SNR per image, green lines stand for the 2-D-SNR after denoising with $L_2L_2 \log$ model, and red lines stand for the 2-D-SNR after denoising with $TVL_2 \log$ model.

TABLE III

SYNTHETIC DATA. THE 2-D+TIME SEQUENCES ARE TAKEN AS 3-D ENTITIES AND THE 3-D-SNR IS COMPUTED BEFORE AND AFTER APPLYING THE PROPOSED DENOISING ALGORITHMS

Algorithm	sequence	Initial 3D-SNR	Final 3D-SNR
$L_2L_2 \log$	<i>sint1</i>	0.47	12.55
	<i>sint2</i>	10.51	16.94
	<i>sint3</i>	20.53	24.24
$TVL_2 \log$	<i>sint1</i>	0.47	16.14
	<i>sint2</i>	10.51	24.17
	<i>sint3</i>	20.53	32.53

with the $TVL_2 \log$ model are higher than the ones attained with the $L_2L_2 \log$ model, which corroborates the assumption that edge preserving *a priori* potentials are more appropriate to keep discontinuities in the space domain.

Taking each 2-D+image time sequence as a 3-D entity, the 3-D-SNR was computed and the results are presented in Table III. As before, the 3-D-SNR results confirm the better performance of the $TVL_2 \log$ when compared to the $L_2L_2 \log$ model.

B. Model Validation

The $TVL_2 \log$ was compared to five state-of-the-art models: the NaiveGauss Proximal Iteration (Prox-it-Gauss) [13], the Anscombe Proximal Iteration (Prox-it-Ans) [13], the NonLocal Means (NLM) [45], the Bivariate-Shrinkage for Wavelet-based denoising (BiShrink) [46] and the Bilateral Filtering (BLF) [47].

Now we give a short description of these algorithms.

The Prox-it-Ans is a deconvolution algorithm for data that is blurred and degraded by Poisson noise. The Anscombe transform used explicitly in the problem formulation, results in a nonlinear convex, AWGN deconvolution problem in the Bayesian framework, with a nonsmooth sparsity-promoting penalty over the representation coefficients in a dictionary of transforms (curvelets, wavelets) of the image to be restored. The solution is obtained by using a fast proximal backward-forward

splitting iteration algorithm. The prior parameter is selected using the generalized cross validation (GCV) criterion.

The Prox-it-Gauss is a naive version of the Prox-it-Ans where the Anscombe transform is performed first. The data are then processed using a model similar to the previous one but where the nonlinearity of the Anscombe transform is not taken into account.

The Nonlocal Means algorithm (NLM) [45] is a nonlocal averaging technique, operating on all pixels in the image with the same characteristic. The NLM can be regarded as an evolution of the Yaroslavski filter [48], where the average is performed among similar pixels in the image and the measure of similarity is based upon the local intensity. The main difference between this filter and the NLM is the way the similarity is measured; the latter is more robust, since it not only compares the gray intensity level in a single point, but also the geometric configuration in a whole neighborhood. The authors also proved that the NLM is asymptotically optimal under a generic statistical image model. For this comparison purpose we have implemented the algorithm in a 3-D version programmed in C++ running in Matlab.

The BLF [47] is a 2-D algorithm that smooths images but preserves edges by means of a nonlinear combination of nearby image values. The method is noniterative, local, simple, and fast. It combines gray levels based upon their geometric closeness and their photometric similarity; it gives preference to near values in both domain and range.

The BiShrink is a locally adaptive 3-D image denoising algorithm using dual-tree complex wavelet transforms with the bivariate shrinkage thresholding function improved by taking into account the statistical dependencies among the representation coefficients. In the present case, the algorithm was employed under the naive Gaussian hypothesis.

The synthetic sequence *sint2* was processed with the proposed $TVL_2 \log$ algorithm and with the five algorithms described previously. Since the proposed algorithm does not comprise deconvolution, the image sequence is processed without any blur.

In model $TVL_2 \log$, the regularization parameters α and β were made to vary from image to image according to (44) and (45). For comparison purposes and whenever possible, the parameters of the models were also adjusted from image to image to take into account the decreasing of intensity along the sequence, in order to obtain the best results.

We use the Csisz  r I-divergence [49] (I-div) and the SNR as figures-of-merit computed for each image for the comparison purposes and the results are shown in Figs. 11 and 12. It is evident in these plots the superior performance of the proposed $TVL_2 \log$ algorithm concerning the SNR and the I-divergence. The SNR curve presents higher values than the other algorithms. As expected, the I-divergence measure, which is very appropriate in the case of the Poisson denoising, is lower than the one computed for the comparison models. Another relevant feature that can be observed in these figures is the smoothness of the curves corresponding to algorithm implemented in 3-D.

Taking the 2-D+time sequence *sint2* as a 3-D entity, the 3-D-SNR and the 3-D-I-div per image pixel were computed after denoising with the six algorithms with the results presented

TABLE IV
SYNTHETIC SEQUENCE *sint2*. DIMENSIONALITY OF THE ALGORITHM,
CPU TIME TO PROCESS THE 64 IMAGES OF THE SEQUENCE,
3-D-SNR AND 3-D-I-DIV *per pixel*

Algorithm		CPU time (s)	3D-SNR (dB)	3D-I-div <i>per pixel</i>
Initial			10.51	0.456
Prox-it-Ans	2D	17577.0	13.77	0.211
Prox-it-Gauss	2D	7032.3	14.73	0.304
BLF	2D	21.9	16.85	0.193
BiShrink	3D	40.3	18.60	0.206
TVL_2 log	3D	37.3	24.17	0.0927
NLM	3D	3983.2	16.77	0.232

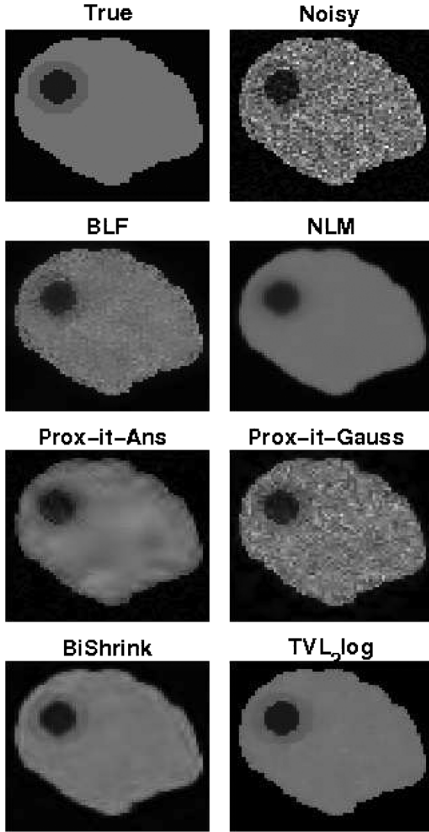


Fig. 9. Image 5 from sequence *sint2*: true, noisy, denoised with the BLF, NLM, Prox-it-Ans, Prox-it-Gauss, BiShrink, and TVL_2 log algorithms.

in Table IV. As before, the TVL_2 log algorithm attains the best results with to the adopted denoising quality measures.

A plot of the relative error based measure described previously and used as stopping criteria is shown in Fig. 10. As can be noticed the proposed algorithm presents good convergence characteristics.

The proposed algorithm has low computational draw. All the algorithms were executed under the same hardware conditions and the TVL_2 log is the second fastest as can be seen in Table IV.

One of the images of the sequence *sint2* is displayed in Fig. 9 in its true, noisy and denoised versions with the TVL_2 log and the other five comparison algorithms. The observation of this figure reinforces the assertions on the ability of the TVL_2 log to remove noise.

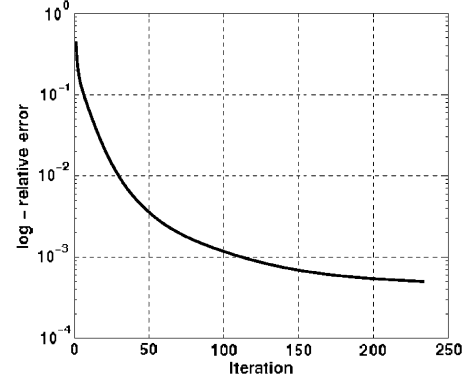


Fig. 10. Synthetic data: *sint2*. Convergence curve of the iterative TVL_2 log algorithm using the relative error $\text{rel. error} = \|z^k - z^{k-1}\| / \|z^k\|$.

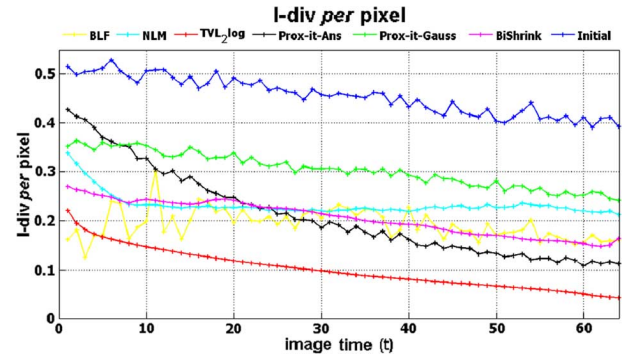


Fig. 11. Synthetic data: *sint2*. 2-D-Csiszár I-divergence of all the algorithms per pixel versus image time (t).

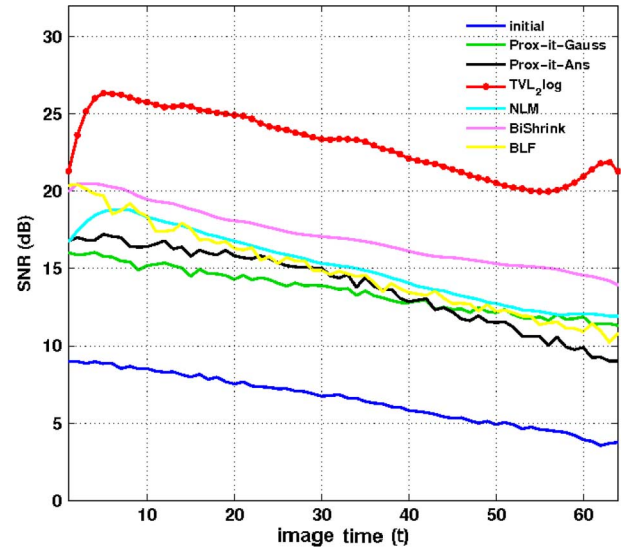


Fig. 12. Synthetic data: *sint2*. 2-D-SNR of all the algorithms versus image time (t).

C. Real Data

In human cells, the messenger ribonucleoproteins (mRNP) after being released from the transcription sites and distributed throughout the nucleoplasm, must reach the nuclear pore complexes (NPC), in order to be translocated to the cytoplasm. To study the nature of this transport, quantitative photobleaching methods can be used in order to investigate the mobility of

TABLE V

REAL IMAGE SEQUENCES. NAME, NUMBER OF IMAGES (N.Im.), AND IMAGE SIZE FOR EACH REAL SEQUENCE. THE CPU TIME *per* ITERATION, THE NUMBER OF ITERATIONS AND THE RELATIVE ERROR BOUND (STOPPING CRITERION) TO PROCESS THE SEQUENCES USING $TV L_2 \log$ ALGORITHM ARE ALSO DISPLAYED

Real data	N.Im.	Image size	CPU (s)/iter.	#Iter.	Error bound
LSM2	216	217×182	2.66	520	5×10^{-5}
noDrug	273	130×190	2.17	389	5×10^{-5}
FLIP1	501	120×120	4.23	499	5×10^{-5}

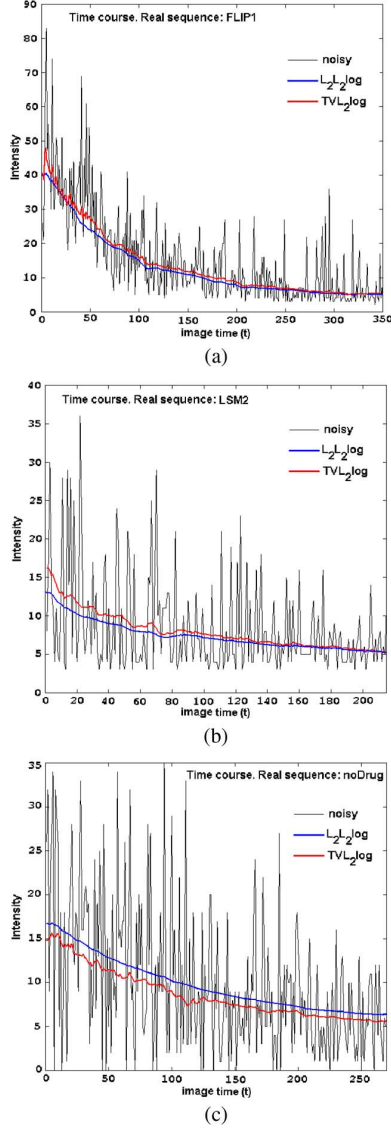


Fig. 13. Time courses. Raw and denoised data with $L_2 L_2 \log$ and $TV L_2 \log$ algorithms of HeLa immortal cell nucleus image sequences: (a) FLIP1. (b) LSM2. (c) noDrug.

mRNP's within the nucleus of the human living cells. FLIP can be an appropriate choice to accomplish this assignment.

In this experiment, RNP complexes were made fluorescent by transient expression of GFP fused to two distinct mRNA-binding proteins: PABPN1 and TAP [50], [51]. The HeLa cell [52] was used.

Cells were repeatedly bleached at intervals of 3.64 s and imaged between pulses. Bleaching was performed by 279 ms

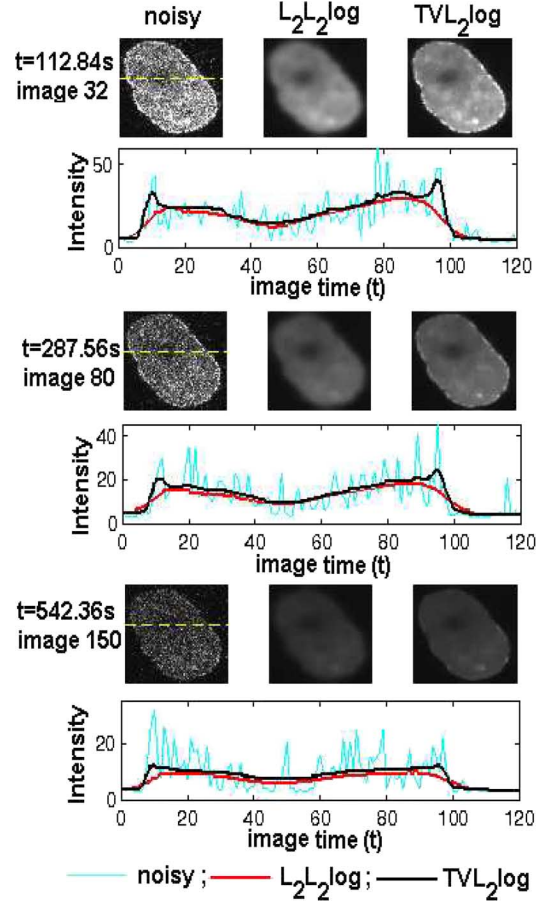


Fig. 14. Real sequence: FLIP1. Raw data (Noisy), denoised data and profile plots of HeLa immortal cell nucleus for images 32, 80, 150 (image acquisition rate = 3.64 s). In the profile plots taken along the yellow dashed line, the cyan line stands for the raw data, the red line for the $L_2 L_2 \log$ model results, and the black line for $TV L_2 \log$ model.

bleach pulses on a spot of $1.065 \mu\text{m}$ radius (30 pixels diameter). Three cell nucleus image sequences, identified as LSM2, noDrug and FLIP1 are used to illustrate the application of the proposed algorithms. The number of images and the image size in the respective sequence are displayed in Table V.

Each sequence of real data is represented by a 3-D tensor \mathbf{Y} , as described in Section II. No preprocessing was performed on these images but a simple alignment procedure to correct for cell nucleus displacement during the acquisition process. The alignment consists in a set of rigid body transformations driven by the maximization of the correlation between images, using a wavelet based strategy.

In order to estimate \mathbf{X} , the aligned images were then processed using the described denoising methodologies. The mean and the standard deviation per image of each sequence were computed. For all the three sequences of images several apparently anomalous jumps were detected in the standard deviation plots ultimately due to the refocusing manoeuvres during the acquisition process. This fact is accounted for the regularization parameters α and β as explained in Section IV-A of this section.

The CPU time for both algorithms ($L_2 L_2 \log$ and $TV L_2 \log$) was approximately the same. The CPU time per iteration on a Centrino Duo 2.00 GHz, 1.99 GB RAM processor and the

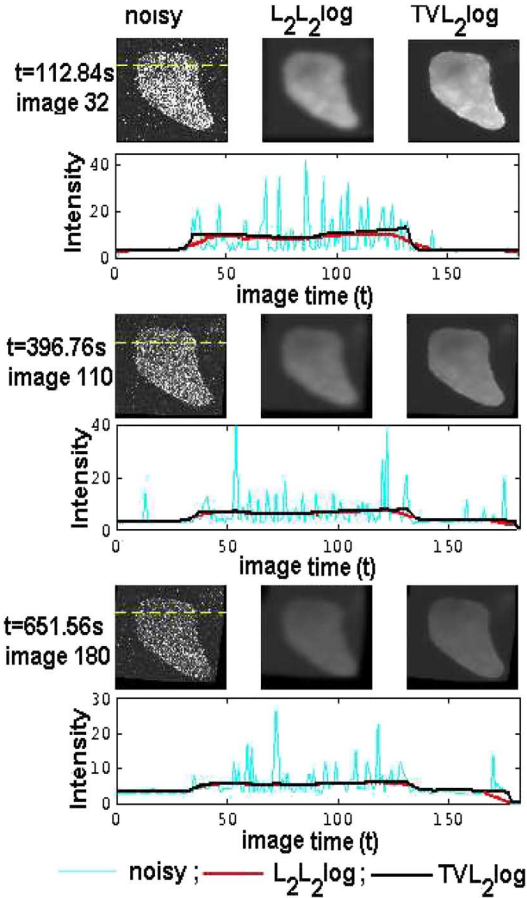


Fig. 15. Real sequence: LSM2: raw data (noisy), denoised data, and profile plots of HeLa immortal cell nucleus for images 32, 110, 180 (image acquisition rate = 3.64 s). In the profile plots taken along the yellow dashed line, the cyan line stands for the raw data, the red line for the L_2L_2 log model results, and the black line for TVL_2 log.

number of iterations required to achieve convergence according to the stopping criterion based upon the relative error bound are displayed in Table V.

The results for three images of each sequence are displayed in Figs. 14–16. From left to right, the first column represents the raw data, the second column represents results with the L_2L_2 log model and third column shows results with the TVL_2 log model. The second, fourth, and sixth rows show cross-section plots of the nucleus at the same time instant as the images in the row above. The observation of these plots, in conjunction with the images, reinforces the conviction that the assumption of an edge preserving *a priori* distribution in the space domain is wise and acceptable. In fact, as can be seen in these figures there is a great deal of improvement in the quality of the representation when using TVL_2 log. The blur present in the denoised images in the second column (L_2L_2 log) results from the log-quadratic regularization used in the space dimension. This undesirable effect is attenuated by using the TV -log instead, which is an *a priori* distribution that presents the ability to preserve the edges.

The denoising performance can also be noticed in the third dimension (time). Results of the denoising with L_2L_2 log and

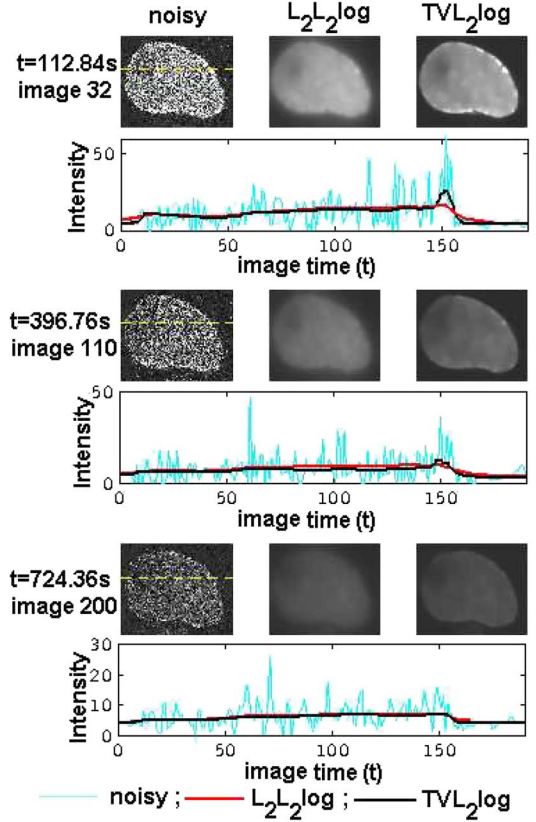


Fig. 16. Real sequence: noDrug: raw data (noisy), denoised data and profile plots of HeLa immortal cell nucleus for images 32, 110, 200 (image acquisition rate = 3.64 s). In the profile plots taken along the yellow dashed line, the cyan line stands for the raw data, the red line for the L_2L_2 log model results, and the black line for TVL_2 log.

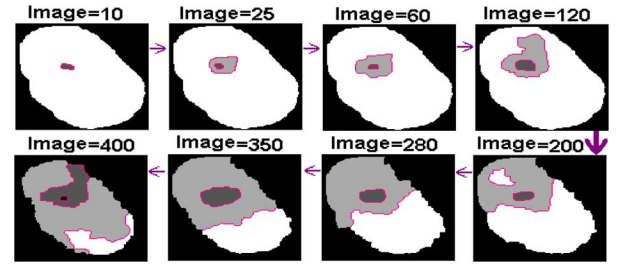


Fig. 17. Real sequence: FLIP1. Segmentation result showing the photo-bleaching propagation across the nucleus from the bleached area in a FLIP experiment. The pink contours represent label level lines. The image acquisition rate is 3.64 s.

TVL_2 log for one time course of each of the nucleus are shown in Fig. 13.

The graph-cuts segmentation procedure described in Section III was performed on the denoised data, using only five labels, in order to display the propagation of the fluorescence loss that occurs inside the nucleus with time in a FLIP experiment. Each gray level represents a range of intensities assigned to a label. The darkest gray region in each image represents the target area hit by the high energy laser pulses. The pink contours represent label level lines and can be regarded as wave fronts to study the diffusion processes that occur inside the nucleus. In addition, this representation gives information on what compartments in the nucleus communicate with each

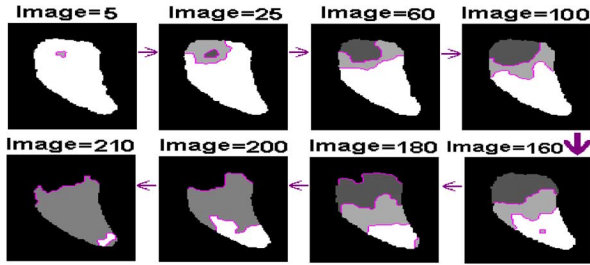


Fig. 18. Real sequence: LSM2. Segmentation result showing the photobleaching propagation across the nucleus from the bleached area in a FLIP experiment. The pink contours represent label level lines. The image acquisition rate is 3.64 s.

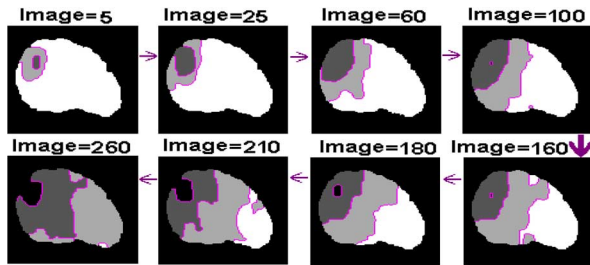


Fig. 19. Real sequence: noDrug. Segmentation result showing the photobleaching propagation across the nucleus from the bleached area. The pink contours represent label level lines. The image acquisition rate is 3.64 s.

other. The segmentation results for some of the denoised images of each cell nucleus are shown in Figs. 17–19. As shown in the figure, the fluorescence loss spreads inside the nucleus from a region around the bleached area toward the edges of the nucleus according to the available connections among nucleus compartments.

V. CONCLUSION

In this paper, two new denoising algorithms are proposed to LSFCM imaging with photobleaching. The sequences of LSFCM images taken along the time courses, in this microscopy genre, are corrupted by a type of pixel dependent noise described by a Poisson distribution. Furthermore, the global intensity of the images decreases along the time courses due to permanent loss of fluorophore ability to fluoresce, caused by chemical reactions induced via the incident laser and by other surrounding molecules. The decreasing image intensity leads to a decrease on the signal to noise ratio of the images, making the biological information recovery a difficult task.

In this paper, two Bayesian algorithms are proposed to perform a simultaneous denoising procedure in the space (images) and in time (time courses) dimensions. This approach, conceived as an optimization task with the MAP criterion, leads to filtering formulations involving 3-D (2-D+time) anisotropic filtering procedures. The energy functions are designed to be convex and their minimizers are computed by using the Newton's method with the L_2L_2 log algorithm and a reweighted least squares based Newton's method with the TVL_2 log algorithm, which allows continuous convergence toward the global minimum, in a small number of iterations.

The significant performance of the approach described in this paper is mainly due to the adoption of a temporal *a priori* distribution with appropriate potential functions that allows to extract relevant information even from small SNR ending images of the sequence that, otherwise, would be useless.

Tests using synthetic and real data have shown the ability of the presented methodology to reduce the pixel dependent noise corrupting the image sequences. Furthermore it is shown that the model TVL_2 log outperforms the L_2L_2 log one because of its edge preserving properties. Comparison tests of the TVL_2 log with five other state-of-the-art algorithms confirm its superior performance because, once again, it outperforms all the other methods, according to the denoising quality measures adopted in this work.

ACKNOWLEDGMENT

The authors would like to thank Dr. J. Rino and Prof. M. do Carmo Fonseca, from the Molecular Medicine Institute of Lisbon, for providing biological technical support and the data used in this paper.

REFERENCES

- [1] J. W. Lichtman and J. A. Conchello, "Fluorescence microscopy," *Nat. Meth.*, vol. 2, no. 12, pp. 910–919, 2005.
- [2] J. A. Schmid and H. Neumeier, "Evolutions in science triggered by green fluorescent protein (GFP)," *ChemBioChem* vol. 6, no. 7, pp. 1149–1156, 2005.
- [3] R. Underwood, "Frap and flip, photobleaching technique to reveal cell dynamics," Nikon Instruments, Melville, NY, 2007 [Online]. Available: http://www.nikoninstruments.com/images/stories/lit-pdfs/nikon_note_3nn06_8_07_lr.pdf
- [4] A. I. L. M. Platani, I. Goldberg, and J. R. Swedlow, "Cajal body dynamics and association with chromatin are atp-dependent," *Nat. Cell Biol.* vol. 4, pp. 502–508, 2002.
- [5] J. Lippincott-Schwartz, N. Altan-Bonnet, and G. H. Patterson, "Photobleaching and photoactivation: Following protein dynamics in living cells," *Nat. Cell Biol.* Sep. 2003.
- [6] J. Berger, *Statistical Decision Theory and Bayesian Analysis*. New York: Springer-Verlag, 1985.
- [7] M. Bertero and P. Boccacci, *Introduction to Inverse Problems in Imaging*. London, U.K.: Inst. Physics, 1998.
- [8] C. Vogel and M. Oman, "Fast, robust total variation-based reconstruction of noisy, blurred images," Penn State, 1998 [Online]. Available: citeseer.ist.psu.edu/vogel98fast.html
- [9] M. Fisz, "The limiting distribution of a function of two independent random variables and its statistical application," in *Proc. Colloq. Math.*, 1955, vol. 3, pp. 138–146.
- [10] P. Fryzlewicz and G. Nason, "Poisson intensity estimation using wavelets and the Fisz transformation," Dept. Math., Univ. Bristol, Bristol, U.K., Tech. Rep. 01/10, 2001.
- [11] R. Willett, "Statistical analysis of photon-limited astronomical signals and images," in *Proc. Statist. Challenges Modern Astron.*, 2006 [Online]. Available: <http://www.ee.duke.edu/~willett/papers/WillettSCMA2006.pdf>
- [12] J.-L. Starck, F. Murtagh, and A. Bijaoui, *Image Processing and Data Analysis, the Multiscale Approach*. Cambridge, U.K.: Cambridge Univ. Press, 1998.
- [13] F.-X. Dupé, J. Fadili, and J.-L. Starck, "A proximal iteration for deconvolving Poisson noisy images using sparse representations," *IEEE Trans. Image Process.*, vol. 18, no. 2, pp. 310–321, Feb. 2009.
- [14] B. Zhang, M.-J. Fadili, and J.-L. Starck, "Wavelets, ridgelets, and curvelets for Poisson noise removal," *IEEE Trans. Image Process.*, vol. 17, no. 7, pp. 1093–1108, Jul. 2008.
- [15] J.-L. Starck, D. L. Donoho, and E. J. Candès, "Very high quality image restoration by combining wavelets and curvelets," *Proc. SPIE*, vol. 4478, pp. 9–19, 2001.
- [16] C. Chaix, J.-C. Pesquet, and N. Pustelnik, "Nested iterative algorithms for convex constrained image recovery problem," *SIAM J. Imag. Sci.*, vol. 2, no. 2, pp. 730–762, Jun. 2009.

- [17] N. Dey, L. Blanc-Féraud, C. Zimmer, Z. Kam, J.-C. Olivo-Marin, and J. Zerubia, "Richardson-Lucy algorithm with total variation regularization for 3-D confocal microscope deconvolution," *Microsc. Res. Tech.*, vol. 69, no. 4, pp. 260–266, 2006.
- [18] G. van Kempen, L. van Vliet, and P. Verveer, "Application of image restoration methods for confocal fluorescence microscopy," in *Proc. SPIE 3-D Microsc. Image Acquisition Process.*, T. W. C. J. Cogswell and J.-A. Conchello, Eds., 1997, vol. 2984, pp. 114–124.
- [19] J. M. Bardsley and A. Luttman, "Total variation-penalized Poisson likelihood estimation for ill-posed problems," *Adv. Computat. Math.*, vol. 31, no. 1–3, pp. 35–59, Oct. 2009.
- [20] J. Besag, "On the statistical analysis of dirty pictures," *J. Roy. Statist. Soc. Ser. B*, vol. 48, no. 3, pp. 259–302, 1986.
- [21] S. Geman and D. Geman, "Stochastic relaxation, Gibbs distributions, and the bayesian restoration of images," *IEEE Trans. Pattern Anal. Mach. Intell.*, vol. PAMI, no. 6, pp. 721–741, Nov. 1984.
- [22] A. Blake and A. Zisserman, *Visual Reconstruction*. Cambridge, MA: MIT Press, 1987.
- [23] T. Hebert and R. Leahy, "A generalized EM algorithm for 3-D bayesian reconstruction from Poisson data using Gibbs priors," *IEEE Trans. Med. Imag.*, vol. 8, no. 12, pp. 194–202, Dec. 1989.
- [24] P. J. Green, "Bayesian reconstructions from emission tomography data using a modified em algorithm," *IEEE Trans. Med. Imag.*, vol. 9, no. 1, pp. 84–93, Jan. 1990.
- [25] S. Geman, D. E. McClure, and D. Geman, "A nonlinear filter for film restoration and other problems in image processing," *CVGIP, Graph. Models Image Process.*, vol. 54, no. 4, pp. 281–289, 1992.
- [26] D. Geman and G. Reynolds, "Constrained restoration and the recovery of discontinuities," *IEEE Trans. Pattern Anal. Mach. Intell.*, vol. 14, no. 3, pp. 367–383, Mar. 1992.
- [27] S. L. Rudin and E. Fatemi, "Nonlinear total variation based noise removal algorithms," *Phys. D*, vol. 60, pp. 259–268, 1992.
- [28] V. Arsigny, P. Fillard, X. Pennec, and N. Ayache, "Log-Euclidean metrics for fast and simple calculus on diffusion tensors," *Magn. Resonance Med.*, vol. 56, no. 2, pp. 411–421, August 2006.
- [29] T. K. Moon and W. C. Stirling, *Mathematical Methods and Algorithms for Signal Processing*. Upper Saddle River, NJ: Prentice-Hall, 2000.
- [30] J. M. Sanches and J. S. Marques, "Joint image registration and volume reconstruction for 3-D ultrasound," *Pattern Recognit. Lett.*, vol. 24, no. 4–5, pp. 791–800, 2003.
- [31] G. Z. V. Panin and G. T. Gullberg, "Total variation regulated EM algorithm," *IEEE Trans. Nucl. Sci.*, vol. 46, no. 6, pp. 2202–2210, Dec. 1999.
- [32] A. Chambolle, "An algorithm for total variation minimization and applications," *J. Math. Imag. Vis.*, vol. 20, no. 1–2, pp. 89–97, 2004.
- [33] J. D. B. J. Sanches and J. S. Marques, "Minimum total variation in 3-D ultrasound reconstruction," in *Proc. IEEE Int. Conf. Image Process.*, Sep. 2005, pp. 597–600.
- [34] J. Bardsley and A. Luttman, "Total variation-penalized Poisson likelihood estimation for ill-posed problems," Dept. Math Sci., Univ. Montana Missoula, Tech. Rep. 8, 2006.
- [35] N. Dey, L. Blanc-Féraud, C. Zimmer, Z. Kam, J.-C. Olivo-Marin, and J. Zerubia, "A deconvolution method for confocal microscopy with total variation regularization," in *Proc. IEEE Int. Symp. Biomed. Imag.: Nano to Macro*, Apr. 2004, vol. 2, pp. 1223–1226.
- [36] C. R. Vogel and M. E. Oman, "Iterative methods for total variation denoising," *SIAM J. Sci. Comput.*, vol. 17, no. 1, pp. 227–238, 1996.
- [37] R. Chan and K. Chen, "Multilevel algorithm for a Poisson noise removal model with total-variation regularization," *Int. J. Comput. Math.*, vol. 84, no. 8, pp. 1183–1198, 2007.
- [38] S. Boyd and L. Vandenberghe, *Convex Optimization*. Cambridge, U.K.: Cambridge Univ. Press, Mar. 2004.
- [39] C. T. Kelley, *Iterative Methods for Optimization*. Philadelphia, PA: SIAM, 1999.
- [40] B. Wohlberg and P. Rodríguez, "An iteratively reweighted norm algorithm for minimization of total variation functionals," *IEEE Signal Process. Lett.*, vol. 14, no. 12, pp. 948–951, Dec. 2007.
- [41] K. P. Bube and R. T. Langan, "Hybrid l^1/l^2 minimization with applications to tomography," *Geophys.*, vol. 62, no. 4, pp. 1183–1195, Jul./Aug. 1997.
- [42] Y. Boykov, O. Veksler, and R. Zabih, "Fast approximate energy minimization via graph cuts," *IEEE Trans. Pattern Anal. Mach. Intell.*, vol. 23, no. 11, pp. 1222–1239, Nov. 2001.
- [43] L. Ford, Jr. and D. Fulkerson, "Maximal flow through a network," *Can. J. Math.*, vol. 8, no. 3, pp. 399–404, Jun. 1956.
- [44] V. Kolmogorov and R. Zabih, "What energy functions can be minimized via graph cuts?," *IEEE Trans. Pattern Anal. Mach. Intell.*, vol. 26, no. 2, pp. 147–159, Feb., 2004.
- [45] A. Buades, B. Coll, and J. M. Morel, "A review of image denoising algorithms, with a new one," *SIAM Multiscale Model. Sim.*, vol. 4, no. 2, pp. 490–530, 2005.
- [46] L. Sendur and W. Selesnick, "Bivariate shrinkage functions for wavelet-based denoising exploiting interscale dependency," *IEEE Trans. Signal Process.*, vol. 50, no. 11, pp. 2744–2756, Nov. 2002.
- [47] C. Tomasi and R. Manduchi, "Bilateral filtering for gray and color images," in *Proc. 6th Int. Conf. Comput. Vis.*, Washington, DC, 1998, p. 839.
- [48] L. Yaroslavsky, *Digital Picture Processing—An Introduction*. New York: Springer-Verlag, 1985.
- [49] I. Csiszár, "Why least squares and maximum entropy? An axiomatic approach to inference for linear inverse problems," *Ann. Statist.*, vol. 19, no. 4, pp. 2032–2066, 1991.
- [50] C. Molenaar, A. Abdulle, A. Gena, H. Tanke, and R. Dirks, "Apoly(a)+rnas roam the cell nucleus and pass through speckle domains in transcriptionally active and inactive cells," *J. Cell Biol.*, vol. 165, pp. 191–202, 2004.
- [51] D. Vargas, A. Raj, S. Marras, F. Kramer, and S. Tyagi, "Mechanism of mrna transport in the nucleus," *Proc. Nat. Acad. Sci. USA*, vol. 102, pp. 17 008–17 013, 2005.
- [52] D. Jackson, F. Iborra, E. Manders, and P. Cook, "Numbers and organization of rna polymerases, nascent transcripts, and transcription units in hela nuclei," *Mol. Biol. Cell*, vol. 9, pp. 1523–1536, 1998.



Isabel Cabrita Rodrigues received the E.E. degree in Physics from the University of Lisbon, Portugal, in 1986, and the M.Sc. degree in applied mathematics to economics and management from the Technical University of Lisbon, Portugal, in 1997.

Currently, she is Assistant Professor in the Electrical, Telecommunications and Computer Engineering Department, Instituto Superior de Engenharia, Lisbon (ISEL), Portugal, and a Researcher at the Institute for Systems and Robotics (ISR). She has taught in the field of mathematics. Her main

research interests are in biomedical engineering, mainly in confocal imaging microscopy mostly in collaboration with several groups from the Medical School at the Hospital de Santa Maria, Lisbon, Portugal.



João Miguel Raposo Sanches (M'06) received the E.E., M.Sc., and Ph.D. degrees from the Technical University of Lisbon, Portugal, in 1991, 1996, and 2003, respectively.

Currently, he is Assistant Professor in the Electrical and Computer Engineering Department, Instituto Superior Técnico, Lisbon (IST), and a Researcher at the Institute for Systems and Robotics (ISR). He has taught in the area of signal processing and control. His main research interests are in biomedical engineering, namely in biomedical

imaging processing and physiological modeling of biological systems with several publications in the field. His research activity is mainly in ultrasound (US), functional magnetic resonance imaging (fMRI), fluorescence confocal microscope (FCM) imaging and neurophysiology, mostly in collaboration with several groups from the Medical School at the Hospital de Santa Maria, Lisbon.

Dr. Sanches is a member of the IEEE Engineering in Medicine and Biology Society and Associate Member of the Bio Imaging and Signal Processing Technical Committee (BISP-TC) of the IEEE Signal Processing Society. He is also president of the Portuguese Association of Pattern Recognition, APRP.